Stierle, E., Vavryčuk, V., Kwiatek, G., Charalampidou, E.-M., Bohnhoff, M. (2016): Seismic moment tensors of acoustic emissions recorded during laboratory rock deformation experiments: sensitivity to attenuation and anisotropy. - *Geophysical Journal International*, *205*, 1, pp. 38—50.

DOI: http://doi.org/10.1093/gji/ggw009

Geophysical Journal International

Geophys. J. Int. (2016) **205,** 38–50
GJI Seismology

doi: 10.1093/gji/ggw009

Seismic moment tensors of acoustic emissions recorded during laboratory rock deformation experiments: sensitivity to attenuation and anisotropy

Eva Stierle,[1] Václav Vavryčuk,[2] Grzegorz Kwiatek,[1] Elli-Maria Charalampidou[3] and Marco Bohnhoff[1,4]

[1] *Helmholtz-Centre, Potsdam German Research Centre for Geosciences (GFZ), Section* 3.2 *Geomechanics and Rheology, Telegrafenberg, D*-14473 *Potsdam, Germany. E-mail: stierle@gfz-potsdam.de*
[2] *Institute of Geophysics, The Czech Academy of Sciences, Boční II*/1401, *Cz*-14131 *Prague, Czech Republic*
[3] *Institute of Petroleum Engineering, School of Energy, Geoscience, Infrastructure and Society, Heriot-Watt University, Edinburgh, Scotland, United Kingdom*
[4] *Freie Universität Berlin, Department of Earth Sciences, Malteser Strasse* 74-100, *D*-12249 *Berlin, Germany*

Accepted 2016 January 7. Received 2016 January 5; in original form 2015 April 17

SUMMARY

Seismic moment tensors can provide information on the size and orientation of fractures producing acoustic emissions (AEs) and on the stress conditions in the sample. The moment tensor inversion of AEs is, however, a demanding procedure requiring carefully calibrated sensors and accurate knowledge of the velocity model. In field observations, the velocity model is usually isotropic and time independent. In laboratory experiments, the velocity is often anisotropic and time dependent and attenuation might be significant due to opening or closure of microcracks in the sample during loading. In this paper, we study the sensitivity of the moment tensor inversion to anisotropy of *P*-wave velocities and attenuation. We show that retrieved moment tensors critically depend on anisotropy and attenuation and their neglect can lead to misinterpretations of the source mechanisms. The accuracy of the inversion also depends on the fracturing mode of AEs: tensile events are more sensitive to *P*-wave anisotropy and attenuation than shear events. We show that geometry of faulting in anisotropic rocks should be studied using the source tensors, since the *P*- and *T*-axes of the moment tensors are affected by velocity anisotropy and deviate from the true orientation of faulting. The stronger the anisotropy is, the larger the deviations are. Finally, we prove that the moment tensor inversion applied to a large dataset of AEs can be utilized to provide information on the attenuation parameters of the rock sample. The method is capable of measuring anisotropic attenuation in the sample and allows for detection of dilatant cracking according to the stress regime.

Key words: Earthquake source observation; Seismic anisotropy; Seismic attenuation; Wave propagation; Acoustic properties.

1 INTRODUCTION

During rock deformation experiments, thousands of acoustic emissions (AEs), are usually observed being caused by microfracturing inside the rock. They display source mechanisms similar to natural earthquakes (Ohtsu 1991; Lockner 1993; Graham *et al*. 2010; Kwiatek *et al*. 2011; Aker *et al*. 2014) but their size is different. AEs are much smaller and radiate much higher frequencies (e.g. Bohnhoff *et al*. 2009, their table 1). Since the rock deformation experiments are conducted under controlled conditions, the AEs are an ideal tool for studying spatio-temporal generation and evolution of fractures and can substantially help in understanding earthquake nucleation and propagation (Lockner 1993; Thompson *et al*. 2006, 2009; Stanchits *et al*. 2011). The processing of AE data is similar to that of earthquake observations. Aside from accurate location of AE hypocentres it is possible to determine fault-plane solutions (Zang *et al*. 2000; Charalampidou *et al*. 2015), to construct and investigate the magnitude–frequency relation and to evaluate the *b*-value (Zang *et al*. 1998), or to perform spatial and temporal analysis of waveforms (Kwiatek *et al*. 2014a). The source processes of AEs can also be studied by moment tensors widely used in earthquake seismology. The moment tensors provide information on the size and orientation of microfractures producing AEs, the slip direction, fracturing mode and ultimately the stress conditions in the sample.

First attempts to apply the moment tensor inversion to AE data were made in hydrofracture tests (Ohtsu 1991) and in studies of

concrete fracturing (Shigeishi & Ohtsu 2001; Finck *et al*. 2003). Graham *et al.* (2010) further compared the moment tensor inversion with the polarity methods developed by Zang *et al*. (1998) and found a concurrent set of results from both methods, similar to what was recently observed by Charalampidou *et al*. (2015). However, moment tensor inversion provides more detailed information about the fracture process in the source. The non-double-couple (non-DC) components of the moment tensors inform us about fracturing mode and physical properties of the rocks (Ohtsu 1991; Julian *et al*. 1998; Vavryčuk 2004, 2005; Aker *et al*. 2014).

The moment tensor inversion is a powerful tool but its application requires high-quality and well-calibrated data. Laboratory experiments should be well designed and amplifications of AE sensors and the coupling effects between the sensors and the rock specimen should be accurately determined. Recently, two new approaches for the sensor calibration were proposed by Davi & Vavryčuk (2012) and Kwiatek *et al*. (2014b). The method by Davi & Vavryčuk (2012) is based on a joint inversion of a set of seismic events for their moment tensors and for sensor amplifications. Kwiatek *et al*. (2014b) used ultrasonic transmission data for assessing the coupling and the sensitivity of the AE sensors as a function of the incidence angle of each ray. Both methods have proven to be efficient in determining or correcting for the sensor amplifications.

Progressive deformation in rock samples results in changes in *P*-wave velocities and attenuation (Stanchits *et al*. 2006; Hamiel *et al.* 2009). Stress-induced attenuation and velocity anisotropy is caused by the formation of microfractures and increases with differential stress. If anisotropy is neglected, the moment tensors are less accurate and can be misinterpreted (Šílený & Vavryčuk 2000, 2002). For example, shear faulting on planar faults produces DC moment tensors in isotropic media, but non-DC moment tensors in anisotropic media (Vavryčuk 2015a). The amount of the non-DC components depends on strength and symmetry of anisotropy and on the orientation of faulting. Since complexity of moment tensors in anisotropic media prevents from their direct interpretation, the analysis of moment tensors must be supplemented by determining source tensors. The source tensors are directly related to geometry of faulting and their interpretation is not biased by anisotropy (Vavryčuk 2005, 2015a).

In this study, we present a moment tensor inversion that accounts for anisotropy in the *P*-wave velocity and attenuation. We develop a joint inversion for the moment tensors of a set of seismic events (or AEs) and for the *P*-wave anisotropic attenuation. The methods are tested on synthetic data and applied to AEs observed during a triaxial compression experiment on a granite sample (Stanchits *et al*. 2006). The derived anisotropic attenuation is compared with that measured using the ultrasonic data. Finally, the moment tensors are used for calculating the source tensors, and the DC and non-DC components of the source tensors are interpreted.

2 THEORY

2.1 Moment tensor inversion

Displacement **u** generated by a seismic point source is calculated using the representation theorem

$$u_i = M_{kl} * G_{ik,l}, \tag{1}$$

where $M_{kl} = M_{kl}(t)$ denotes the seismic moment tensor, $G_{ik,l}$ the spatial derivative of the Green's tensor amplitudes, and symbol '$*$' represents time convolution. Since we invert amplitudes, the convolution in eq. (1) is reduced to multiplication and the moment tensor is obtained as (e.g. Lay & Wallace 1995):

$$\mathbf{m} = \mathbf{G}^{-g}\mathbf{u} \text{ with } \mathbf{G}^{-g} = \left[\mathbf{G}^T\mathbf{G}\right]^{-1}\mathbf{G}^T, \tag{2}$$

where $\mathbf{G}^{-g}$ denotes the generalized linear inversion of **G**. Matrix **G** is the $N \times 6$ matrix of the spatial derivatives of the Green's function amplitudes,

$$\mathbf{G} = \begin{bmatrix} G_1^{(1)} & G_2^{(1)} & G_3^{(1)} & G_4^{(1)} & G_5^{(1)} & G_6^{(1)} \\ G_1^{(2)} & G_2^{(2)} & G_3^{(2)} & G_4^{(2)} & G_5^{(2)} & G_6^{(2)} \\ \dots & \dots & \dots & \dots & \dots & \dots \\ G_1^{(N)} & G_2^{(N)} & G_3^{(N)} & G_4^{(N)} & G_5^{(N)} & G_6^{(N)} \end{bmatrix}, \tag{3}$$

m is the moment vector composed of the six components of the moment tensor **M**,

$$\mathbf{m} = \begin{bmatrix} M_{11} & M_{22} & M_{33} & M_{23} & M_{13} & M_{12} \end{bmatrix}^T, \tag{4}$$

and **u** is the vector of displacement amplitudes observed at *N* sensors,

$$\mathbf{u} = \begin{bmatrix} u^{(1)} & u^{(2)} & \dots & u^{(N)} \end{bmatrix}^T. \tag{5}$$

The spatial derivatives of the Green's function $G_l^{(i)}$ are calculated for the *i*th sensor by:

$$\begin{aligned} &G_1^{(i)} = g_1^{(i)},_1, \quad G_2^{(i)} = g_2^{(i)},_2, \quad G_3^{(i)} = g_3^{(i)},_3, \\ &G_4^{(i)} = g_2^{(i)},_3 + g_3^{(i)},_2, \quad G_5^{(i)} = g_1^{(i)},_3 + g_3^{(i)},_1, \quad G_6^{(i)} = g_1^{(i)},_2 + g_2^{(i)},_1, \end{aligned} \tag{6}$$

where $g_k^{(i)}$ is the amplitude at the *i*th sensor produced by the point force directed along the x_k-axis. The amplitude is calculated for the direction along the sensor axis.

2.2 Green's function in homogeneous anisotropic attenuating media

To determine moment tensor **M** using eq. (2), we have to calculate the Green's function and particularly its spatial derivative $G_{ik,l}$. For anisotropic attenuating media, the Green's function can be calculated using a model of viscoelastic anisotropy. This model describes jointly velocity anisotropy and attenuation by introducing complex-valued, frequency-dependent, viscoelastic parameters (Auld 1973; Carcione 2007; Vavryčuk 2007a,b, 2015b). The real part of the parameters controls the propagation velocity and their imaginary part controls the wave attenuation.

The asymptotic Green's function and its spatial derivative in homogeneous, anisotropic, viscoelastic media reads (Vavryčuk 2007a, his eqs 18 and 19):

$$G_{kl}(\mathbf{x}, \omega) = \frac{1}{4\pi\rho} \frac{g_k g_l}{v\sqrt{|K|}} \frac{1}{r} \exp\left(\mathrm{i}\sigma_0 + \mathrm{i}\omega\, \mathbf{p}_0 \cdot \mathbf{x}\right), \tag{7}$$

$$\frac{\partial}{x_m} G_{kl}(\mathbf{x}, \omega) = \frac{\mathrm{i}\omega}{4\pi\rho} \frac{g_k g_l p_{0m}}{v\sqrt{|K|}} \frac{1}{r} \exp\left(\mathrm{i}\sigma_0 + \mathrm{i}\omega\, \mathbf{p}_0 \cdot \mathbf{x}\right), \tag{8}$$

where

$$\sigma_0 = -\frac{1}{2}(\varphi_1 + \varphi_2), \quad -\frac{3}{2}\pi \le \varphi_1 < \frac{1}{2}\pi, \quad -\frac{3}{2}\pi \le \varphi_2 < \frac{1}{2}\pi,$$

and $\mathbf{p}_0$ is the stationary slowness vector (see Vavryčuk 2007a,b). Quantity $K = K_1 K_2$ is the Gaussian curvature of the slowness surface, K_1 and K_2 are the principal curvatures, and φ_1 and φ_2 are their phase angles. All quantities dependent on slowness

vector **p** are evaluated at stationary point $\mathbf{p}_0$. Position vector $\mathbf{x} = r\mathbf{N}$, distance r, ray vector **N**, frequency ω, phase angles φ_1 and φ_2, and density ρ are real-valued; but polarization vector **g**, Gaussian curvature K, principal curvatures K_1 and K_2, energy velocity v and slowness vector $\mathbf{p}_0$ are complex-valued. The meaning of the complex-valued quantities is discussed in detail in Vavryčuk (2007a).

2.3 Elliptic viscoelastic anisotropy

The wave quantities in eqs (7) and (8) depend on 21 complex-valued viscoelastic parameters. The problem is simplified if we assume elliptic, viscoelastic, anisotropic media, when the slowness surface is spheroidal (Helbig 1994) and the medium is described by two viscoelastic parameters a_{11} and a_{33}. The stationary slowness vector $\mathbf{p}_0$, energy velocity vector **v**, and the Gaussian curvature of the slowness surface K can be expressed as follows (Vavryčuk & Yomogida 1996):

$$\mathbf{p}_0 = \frac{1}{\sqrt{a_{33}N_1^2 + a_{33}N_2^2 + a_{11}N_3^2}} \left[N_1 \frac{a_{33}}{a_{11}},\ N_2 \frac{a_{33}}{a_{11}},\ N_3 \frac{a_{11}}{a_{33}} \right]^T, \tag{9}$$

$$\mathbf{v} = [a_{11}p_{01}, a_{11}p_{02}, a_{33}p_{03}]^T, \tag{10}$$

$$K = \frac{a_{11}^2 a_{33}}{v^4} [a_{11}p_{01}, a_{11}p_{02}, a_{33}p_{03}]^T, \tag{11}$$

where **N** is the real ray direction vector, and v is the complex energy velocity calculated as

$$v = \sqrt{v_i v_i}. \tag{12}$$

For simplicity, the polarization vector of direct P waves in eqs (7) and (8) are identified with the ray direction. The information on phase σ_0 is not important, because we do not analyse phase shifts but only amplitudes.

The quantities in eqs (9)–(12) are expressed using real ray direction **N** and two complex parameters a_{11} and a_{33} describing the elliptic anisotropy. Parameters a_{11} and a_{33} can be determined in a laboratory experiment by measuring velocities and Q-factors (or attenuations) in the horizontal and vertical directions in the sample. Since the ray and phase quantities (velocities and Q-factors) coincide in the horizontal direction as well as in the vertical direction, the parameters a_{11} and a_{33} can be calculated from real ray velocities V_V and V_H, and ray Q-factors Q_V and Q_H as follows (see Vavryčuk 2015b, his eq. 21):

$$a_{11} = V_H^2 \left(1 - \frac{i}{Q_H}\right), \quad \text{and} \quad a_{33} = V_V^2 \left(1 - \frac{i}{Q_V}\right). \tag{13}$$

The vertical and horizontal Q-factors can be determined from the horizontal and vertical attenuations A_H and A_V, which control amplitude decay of waves along the vertical and horizontal rays (Vavryčuk 2008, his eqs 51 and 59)

$$Q_H = \frac{1}{2A_H V_H}, \quad \text{and} \quad Q_V = \frac{1}{2A_V V_V}. \tag{14}$$

2.4 Moment and source tensors

Moment and source tensors are basic quantities defining seismic point sources. The source tensor **D** describes geometry of faulting, and the moment tensor **M** describes body dipole forces acting at the source. The source tensor **D** is expressed as (Ben-Zion 2003; Vavryčuk 2005):

$$D_{kl} = \frac{uS}{2}(s_k n_l + s_l n_k), \tag{15}$$

where unit vectors **n** and **s** denote the crack normal and the direction of the slip vector, u is the slip magnitude, and S is the crack area. If vectors **n** and **s** are perpendicular (the slip vector is along the crack), the source tensor is double couple and describes shear faulting.

The moment tensor **M** is calculated from the source tensor **D** and elastic stiffness parameters c_{ijkl} using the generalized Hooke's law

$$M_{ij} = c_{ijkl} D_{kl}. \tag{16}$$

In anisotropic media, the source and moment tensors diagonalize in different systems of eigenvectors, called the P_M, N_M and T_M axes for the moment tensors, and the P_S, N_S and T_S axes for the source tensors.

In isotropic media, eq. (16) is expressed using Lame's coefficients λ and μ as

$$M_{ij} = \lambda D_{kk}\delta_{ij} + 2\mu D_{ij}, \tag{17}$$

and the eigenvectors of the source and moment tensors are identical, called simply the P-, N- and T-axes (pressure, neutral and tension axes).

If moment tensor **M** is known, the source tensor **D** is calculated by inverting eq. (16):

$$D_{ij} = S_{ijkl} M_{kl}, \tag{18}$$

where S_{ijkl} are the elastic compliance parameters determined from elastic stiffness parameters c_{ijkl} as described, for example, in Auld (1973).

Eq. (17) indicates that a straightforward interpretation of moment tensors in terms of faulting geometry is possible in isotropic media only. For example, shear faulting in isotropic media is represented by the standard DC moment and source tensors. In anisotropic media, the source tensor of shear faulting is still double couple (see eq. 15). However, the moment tensor becomes more complicated being affected not only by geometry of faulting but also by material properties in the focal zone (see eq. 16). The moment tensors can take a general form with non-zero isotropic (ISO), DC and compensated linear vector dipole (CLVD) components even for simple shear faulting on a planar fault (Vavryčuk 2004, 2015a). Therefore, geometry of faulting of AEs in anisotropic media should be determined from the DC and non-DC components of the source tensors.

3 SETUP OF THE EXPERIMENT

We analyse AE data collected by Stanchits *et al.* (2006) during triaxial compression experiments on a granite sample. The cylindrical sample (diameter 50 mm, length 100 mm) was subjected to three differential stress cycles at successively decreasing confining pressure of 60, 40 and 20 MPa, respectively. During the two first stress cycles, the sample was loaded by axial vertical compression up to a maximum axial load of 500 MPa. During the lowest confining pressure cycle, the sample was loaded up to macroscopic failure. AE activity

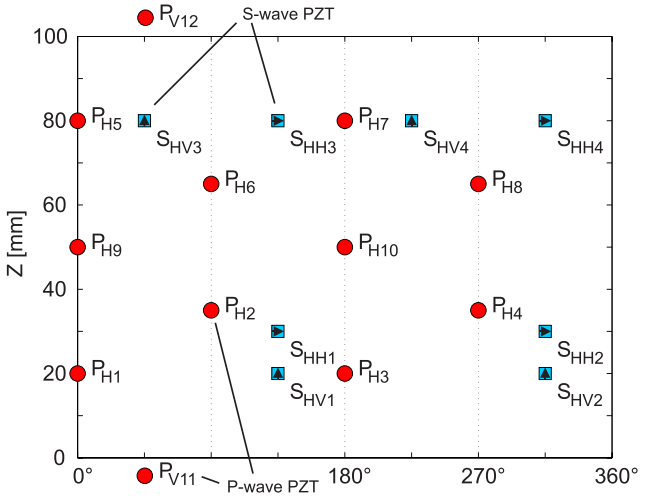

Figure 1. Projected sample surface with positions of 20 ultrasonic sensors as a function of azimuth (in the horizontal plane) and vertical coordinate z. P_H and P_V are the piezoelectric sensors measuring the P-wave velocity in the horizontal and vertical directions. S_{HH} are the shear sensors polarized in the horizontal direction, S_{HV} are the shear sensors polarized in the vertical direction.

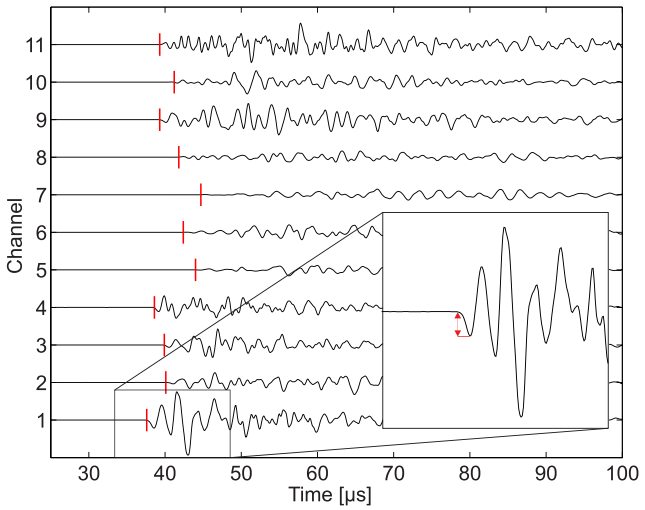

Figure 2. Waveform recordings of an acoustic emission event generated during a laboratory rock-deformation experiment. Channels indicate individual sensors glued onto the deformed rock specimen. Red vertical lines mark automatically picked P-wave arrivals. The inset shows the enlarged P wave of sensor 1 with the arrow indicating how P-wave amplitudes were measured.

and velocity changes were monitored by twelve P-wave and eight S-wave piezoelectric sensors (Fig. 1) with a sampling frequency of 10 MHz. We analysed the P-wave data only, since the S-wave data were contaminated by strong coda waves (Fig. 2). The axial loading rate was servo-controlled using the AE control. For repeated P-wave velocity measurements, six P sensors and four S sensors were used as emitters by applying 100 V pulses every 30–40 s during loading and the remaining sensors were recording the transmitted signals. Two pairs of strain gages were glued directly onto the sample surface for calculating the volumetric strain (global measurement). The ultrasonic measurements of the P-wave velocity revealed that the originally isotropic sample became anisotropic under axial loading. The P-wave velocity markedly decreased in the horizontal direction and slightly increased in the vertical direction while the axial loading was increasing (Fig. 3). After unloading, the sample became again almost isotropic. Stanchits *et al.* (2006) analysed AEs and distinguished between the T- (tensile), C- (compaction) and S-type (shear) events according to the observed polarities of the P waves. With increasing axial stress, the T-type events were dominant. Close to failure, the S-type events became increasingly important.

The loading cycles at 60, 40 and 20 MPa produced a different level of damage of the sample and different anisotropy strength during loading. The most extreme changes were observed for the loading cycle at 20 MPa. The rock sample was loaded until macroscopic failure and therefore highly damaged and inhomogeneous. Strength of the P-wave anisotropy increased up to 50 per cent before the failure. The complex structure with extensive fracture systems produced a complicated scattered wave field difficult to interpret and invert for moment tensors. Therefore, we focused on the loading cycle at 40 MPa where the rock sample remained homogeneous and was weakly damaged. The strength of anisotropy developed during the loading cycle was high enough (P-wave anisotropy strength increased up to 24 per cent, see Fig. 3a) to produce detectable effects in the wave field and the waveforms of AEs. The waveforms of AE were interpreted with no major problems and the moment tensor inversion worked safely.

We applied a method of Stanchits *et al.* (2003, their eq. 3) to calculating vertical and horizontal attenuations in the sample from ultrasonic transmission data. We selected sensors PV11 and PV12 for estimating the vertical attenuation and sensors PH9 and PH10 for estimating the horizontal attenuation (Fig. 1). The measurements do not allow estimating absolute values of attenuation. However, we were able to determine the temporal evolution of the relative values of attenuation from repeating measurements. The vertical attenuation (parallel to axial stress) was decreasing due to the closure of the horizontal microcracks and the compacted pore space, while the horizontal attenuation was increasing due to the opening of vertically oriented, dilatant microcracks (Fig. 3d).

4 SYNTHETIC TESTS

Prior to analysis of observations of AEs, we performed synthetic tests to assess the accuracy of the moment and source tensor inversions for a given experimental setup. We focused on studying the sensitivity of the retrieved moment and source tensors to anisotropy and attenuation of a rock sample and evaluated errors produced by the inversion when anisotropy or attenuation are neglected.

4.1 Sensor configuration and model of the medium

The sensor configuration and the locations of events were taken from the laboratory experiment (Figs 1 and 4). We selected a subset of 429 events located in the centre of the sample to ensure good azimuthal coverage of sensors on the focal sphere (Fig. 4b) needed for a stable moment tensor inversion.

In forward and inverse modelling of moment tensors we employed the Green's function for elliptic, anisotropic, attenuating media (see Sections 2.2 and 2.3). To evaluate the sensitivity of source and moment tensors to velocity anisotropy and attenuation we assumed three alternative medium models:

(1) Anisotropic attenuating model: defined by time-dependent velocity and attenuation anisotropy consistent with ultrasonic measurements in the experiment. The horizontal and vertical velocities

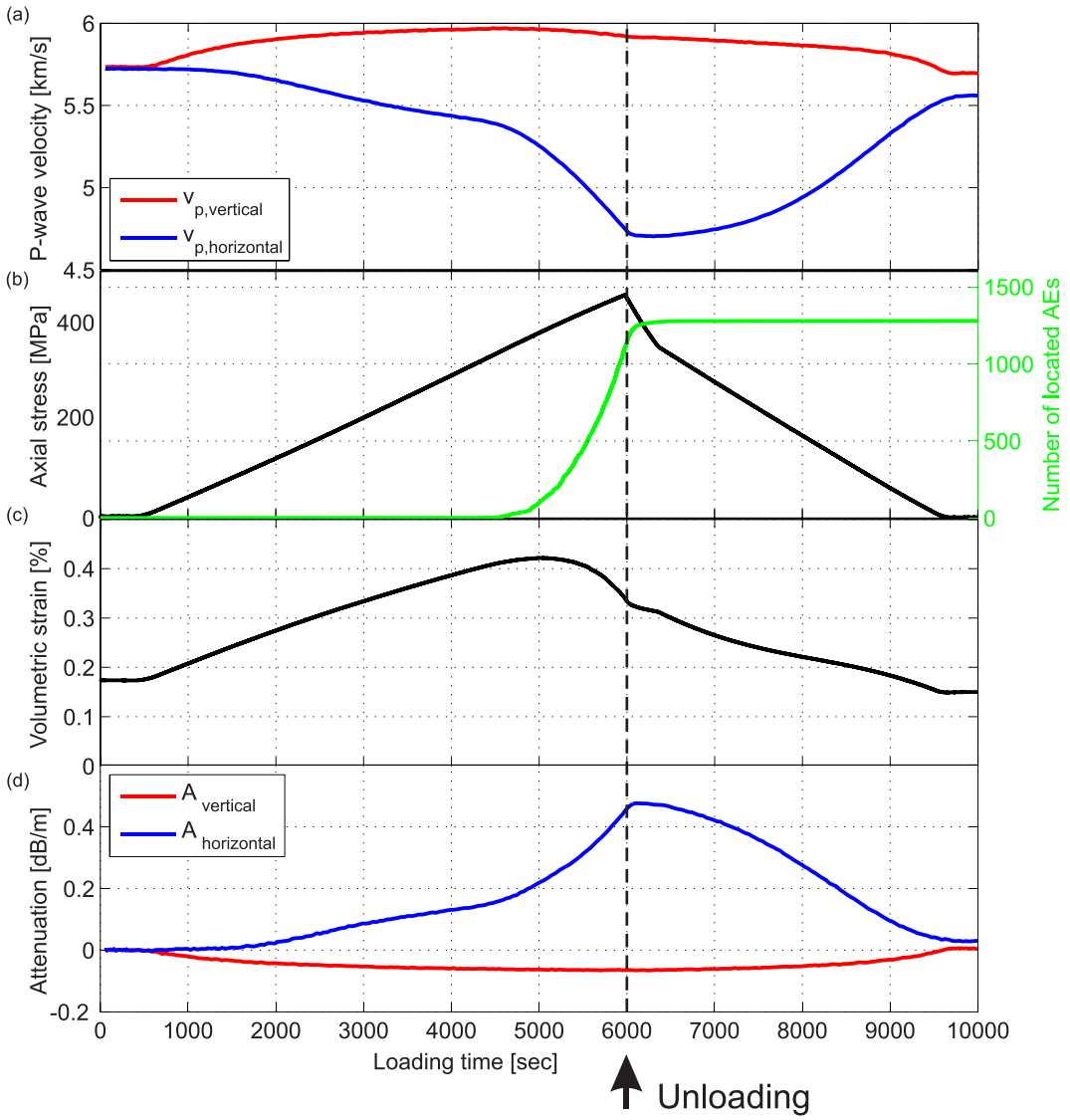

Figure 3. (a) Vertical (measured by sensors 11–12) and horizontal (measured by sensors 9–10) *P*-wave velocities, (b) applied axial stress and acoustic emission rate and (c) volumetric strain measured by Stanchits *et al*. (2006). Plot (d) shows the relative horizontal attenuation measured by sensors 9–10 (blue line) and vertical attenuation measured by sensors 11–12 (red line) derived from ultrasonic transmission data after Stanchits *et al*. (2003, their eq. 3). The confining pressure was 40 MPa during the loading cycle.

are shown in Fig. 3(a). The horizontal and vertical attenuations A_H and A_V follow the time dependence of the relative attenuation measurements shown in Fig. 3(d). The relative attenuation was scaled to start at the value of 3.4×10^{-3} s km^{-1}. During loading, the horizontal attenuation increased up to 5.6×10^{-3} s km^{-1} but the vertical attenuation decreased down to 3.2×10^{-3} s km^{-1}. Since the velocity and attenuation anisotropy was time dependent during the loading cycle, the model was specified for individual AEs according to their origin time.

(2) Isotropic attenuating model: obtained from the anisotropic attenuating model by neglecting the velocity anisotropy. Instead, a constant directionally independent *P*-wave velocity of 5.2 km s^{-1} was assumed.

(3) Anisotropic elastic model: obtained from the anisotropic attenuating model by neglecting attenuation. The parameters of the velocity anisotropy remained unchanged.

The anisotropic attenuating model is the true model used for calculating synthetic amplitudes imitating observations of AEs. The anisotropic elastic and isotropic attenuating models are used in the moment tensor inversions for assessing the sensitivity of moment tensors to velocity anisotropy and attenuation of the medium.

4.2 Source model of AEs

The sources of AEs were calculated using the tensile-source model (see Fig. 5). The crack normal **n** and the slip direction **s** in this model are defined by strike ϕ, dip δ, rake λ and slope α as follows (Vavryčuk 2011):

$$n_1 = -\sin\delta\sin\phi,$$
$$n_2 = \sin\delta\cos\phi,$$
$$n_3 = -\cos\delta, \qquad (19)$$

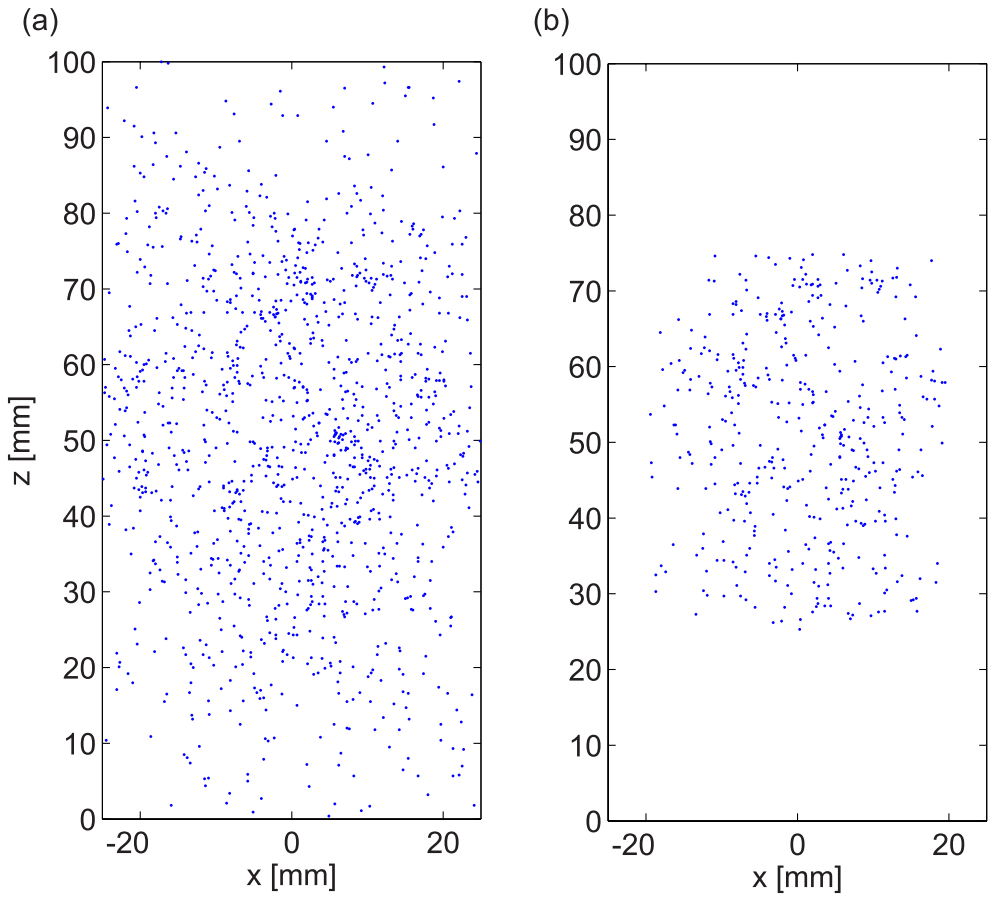

Figure 4. Locations of AEs plotted in the x–z projection for: (a) all 1278 events and (b) the selected subset of 429 events, covering the inner part of the sample.

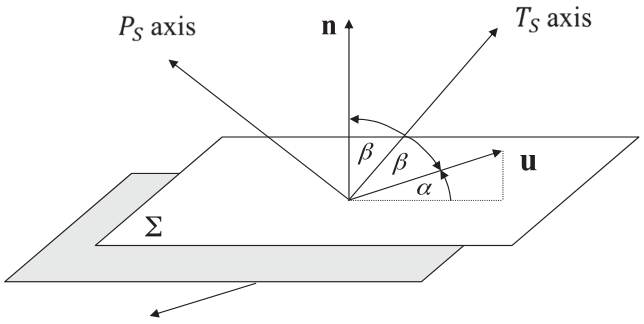

Figure 5. Model of a tensile source. Σ is the plane of crack, **u** is the slip vector, **n** is the crack normal, and α is the slope angle defined as the deviation of slip vector **u** from the plane of crack. Angle β is $\beta = (\alpha - 90^\circ)/2$. The P_S- and T_S-axes are the eigenvectors of the source tensor and are mutually perpendicular. For details, see Vavryčuk (2011).

and

$$s_1 = (\cos\lambda\cos\phi + \cos\delta\sin\lambda\sin\phi)\cos\alpha - \sin\delta\sin\varphi\sin\alpha,$$
$$s_2 = (\cos\lambda\sin\phi - \cos\delta\sin\lambda\cos\phi)\cos\alpha + \sin\delta\cos\phi\sin\alpha,$$
$$s_3 = -\sin\lambda\sin\delta\cos\alpha - \cos\delta\sin\alpha. \quad (20)$$

This source model allows the cracks to be opened or closed during shear failure at the source. The inclination of the slip vector from the plane of a crack is called the slope angle. The slope ranges from –90° to 90°. It is positive for tensile events (opening cracks) and negative for compressive events (closing cracks). If its absolute value is small, the source is predominantly shear. Source tensor **D** is calculated from vectors **n** and **s** using eq. (15). Moment tensor **M** is obtained from source tensor **D** and elastic parameters of the medium using eq. (18).

We generated two synthetic datasets: one contained pure shear events and the other tensile events. To model the source mechanisms of AEs representative for the triaxial loading experiments we chose shear events with dips from 30° to 60°, rakes from –120° to –50° and strikes from 0° to 360°, and tensile events with dips from 45° to 60°, rakes from –100° to –70° and strikes from 0° to 360°. The slope angle is 0° for shear events and between 25° and 26° for tensile events. The non-DC content (ISO + CLVD) of moment tensors of tensile events is about 60 per cent (calculated according to the standard decomposition formulas of Vavryčuk 2015a).

The synthetic P-wave amplitudes at each sensor were calculated using eq. (1) from the moment tensors of shear or tensile events and from the spatial derivatives of the Green's function for the true anisotropic attenuating medium. The synthetic amplitudes served as the 'observed' data for the moment tensor inversion using eq. (2).

4.3 Analysis of shear AEs

The P-wave amplitudes of shear AEs were inverted for the moment and source tensors assuming: the anisotropic attenuating medium, the isotropic attenuating medium, and the anisotropic elastic medium (Fig. 6). The results are shown using the P- and T-axes on the focal sphere and the non-DC components in the diamond CLVD-ISO plots. To assess the quality of the retrieved moment

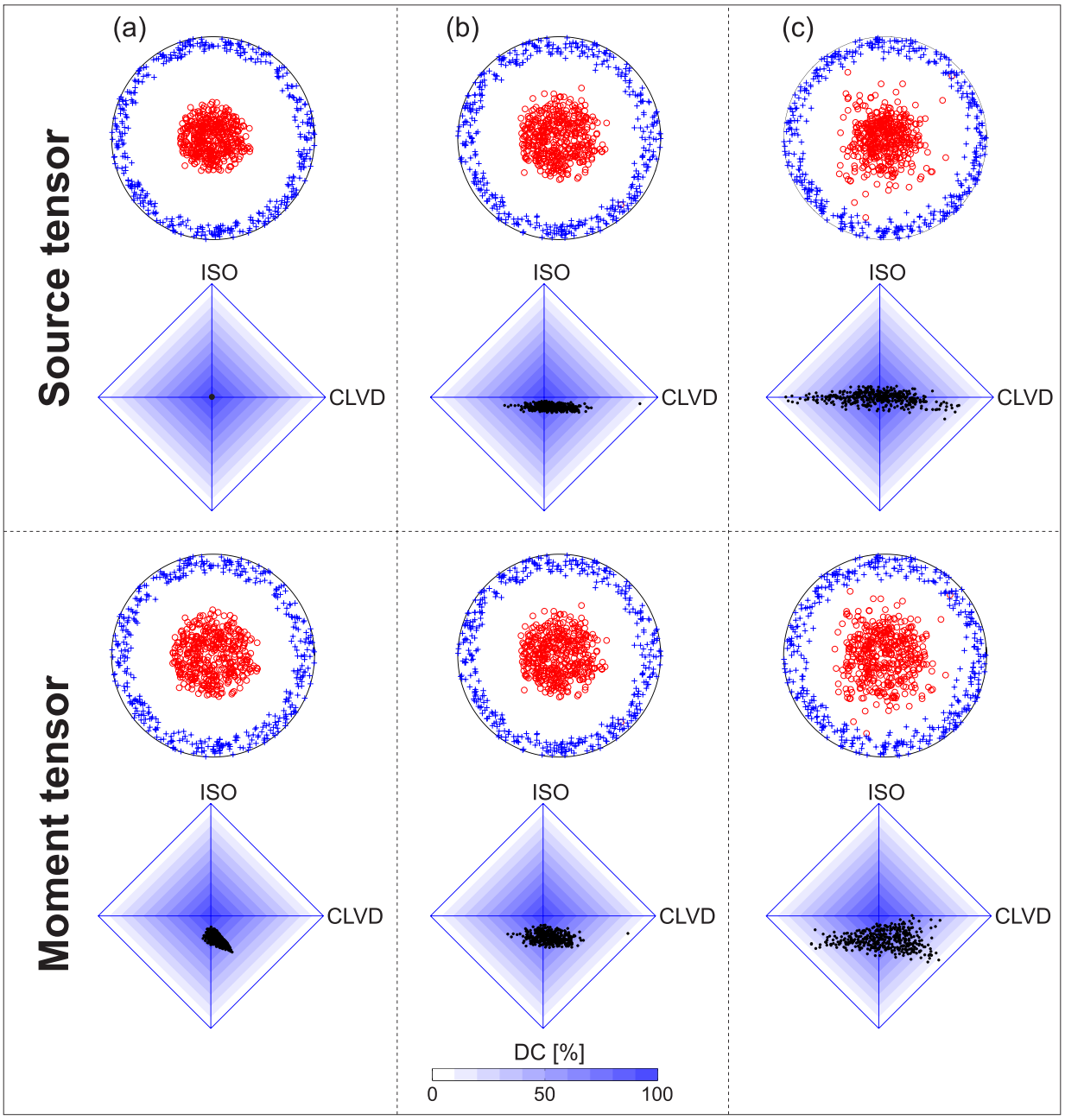

Figure 6. Synthetic tests of the moment and source tensor inversions of shear AE events. The *P*-axes (red circles in focal spheres) and *T*-axes (blue plus signs in focal spheres) and the non-DC components (black dots in diamond plots) are calculated for the source tensors (upper plots) and moment tensors (lower plots) of AEs in (a) anisotropic attenuating model, (b) isotropic attenuating model and (c) anisotropic elastic model.

tensors the normalized rms error between theoretical and observed amplitudes is determined using the following formula:

$$\mathrm{rms} = \frac{\sqrt{\sum_{i=1}^{N}\left(A_i^{\mathrm{obs}} - A_i^{\mathrm{theor}}\right)^2}}{\sqrt{\sum_{i=1}^{N}\left(A_i^{\mathrm{obs}}\right)^2}} \qquad (21)$$

where A^{theor} are the theoretical amplitudes predicted by the retrieved moment tensor, and A^{obs} are the synthetic amplitudes imitating observations. Subscript i is the sequential number of the sensor, and N is the total number of sensors at which the amplitudes were recorded for the respective event.

If the true anisotropic attenuating medium is used for calculating the Green's function in the inversion, the retrieved moment and source tensors are correct (Fig. 6a) and the rms is zero. The P_S- and T_S-axes (i.e. the source tensors *P*- and *T*-axes) reflect the true geometry of faulting (see eq. 15). If the medium is mismodelled by using the isotropic attenuating model (Fig. 6b) or anisotropic elastic model (Fig. 6c), the P_S- and T_S-axes as well as the P_M- and T_M-axes found in the inversion are similar to the true P_S- and T_S-axes. Hence, the orientation of faulting is described adequately by the *P*- and *T*-axes of both tensors regardless of the velocity and attenuation model considered in the inversion.

The non-DC components of the source and moment tensors behave differently. They are zero for true source tensors (Fig. 6a,

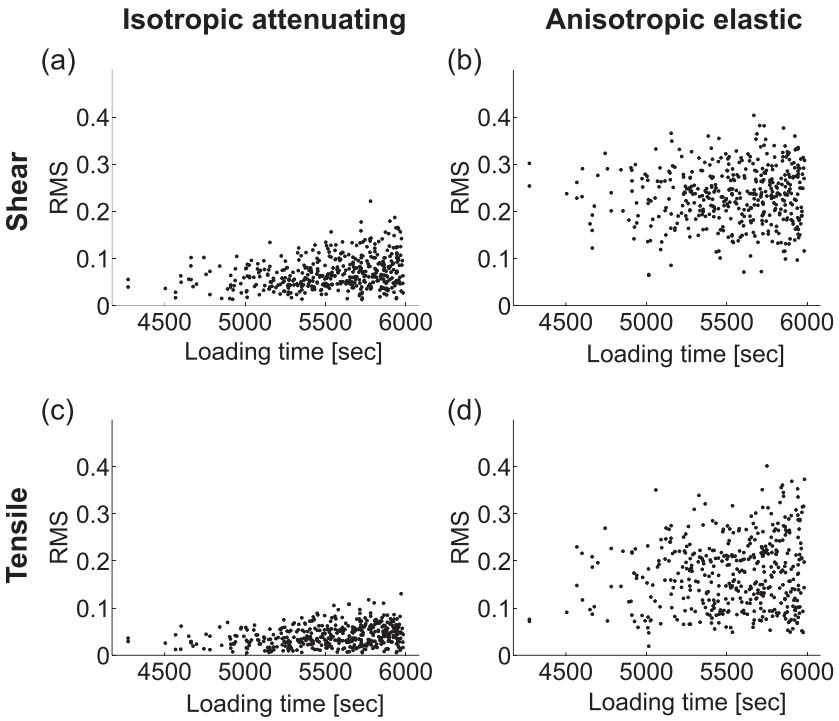

Figure 7. Root-mean-square (rms) values of the moment tensor inversion of synthetic shear (a,b) and tensile (c,d) AEs produced by mismodelling of the medium. The inversion is performed in: (a,c) the isotropic attenuating medium and (b,d) the anisotropic elastic medium.

upper CLVD-ISO plot) but non-zero for true moment tensors (Fig. 6a, lower CLVD-ISO plot). The non-DC components of true moment tensors are produced by the velocity and attenuation anisotropy in the focal zone (see eq. 16). The upper CLVD-ISO plots in Figs 6(b) and (c) document that the velocity mismodelling by neglecting anisotropy or attenuation produces false non-DC components in the source tensors. In particular, the CLVD component is affected and the errors are about three times larger than those of the ISO component. Also, the retrieved non-DC components are biased and more scattered than the true ones (Fig. 6, lower CLVD-ISO plots).

If the velocity anisotropy is neglected, the rms values increase with proceeding deformation. Anisotropy becomes stronger during the loading cycle and the assumption of an isotropic medium becomes more inadequate (Fig. 7a).

4.4 Analysis of tensile AEs

A dataset of tensile AEs was analysed analogously to the shear AEs. Again, the source tensors for the anisotropic attenuating medium (Fig. 8a, upper plot) describe the true faulting geometry of the events. The distribution of the P_M- and T_M-axes shows that moment tensors of tensile events (Fig. 8a, lower plot) are more sensitive to anisotropy than those of shear events (Fig. 6a, lower plot). The P_M- and T_M-axes are remarkably different from the P_S- and T_S-axes and cannot easily be interpreted in terms of geometry of faulting.

When the *P*-wave amplitudes are inverted assuming the isotropic attenuating model, the clustering of the P_S- and T_S-axes is lost due to velocity mismodelling (Fig. 8b, upper plot). The uncertainties are high and the interpretation of faulting parameters from the source tensors becomes impossible. By contrast, neglecting attenuation does not influence significantly the directions of the retrieved P_S- and T_S-axes (Fig. 8c, upper plot). Their deviations from the true directions are small.

Focussing on the non-DC components, the sensitivity to neglecting anisotropy or attenuation is similar for moment and source tensors. The retrieved non-DC components are biased and more scattered than the true ones. Especially, the CLVD component is sensitive to mismodelling of the medium, because the errors are about three times larger than those of the ISO (Figs 8b and c). In general, the sensitivity of the non-DC components of tensile events is comparable to that of shear events.

4.5 Inversion for anisotropic attenuation

We examined whether observations of AEs could jointly be inverted for moment tensors and attenuation of the medium. The synthetic dataset was created analogously to the previous datasets of tensile AEs, except for the value of the slope angle. While the range of the slope was very narrow in the previous tests (between 25° and 26°), here the slope ranged from –10° to 25°. These values were found in the analysis of observed AEs. The true vertical and horizontal attenuations A_V and A_H were 3.4×10^{-3} and 5.6×10^{-3}, respectively. To simulate realistic observations of AEs, we contaminated synthetic amplitudes with uniformly distributed, random noise with a noise level up to 30 per cent of the amplitude at the respective sensor.

We repeatedly inverted the synthetic data of tensile AEs for their moment tensors assuming various velocity models. We fixed velocity anisotropy (taken from the experiment, see Fig 3a) and varied horizontal and vertical attenuations. In the inversion, we simplified the problem assuming attenuation to be time-independent. The optimum horizontal and vertical attenuation values have been found by minimizing the mean rms of all events in a grid with horizontal

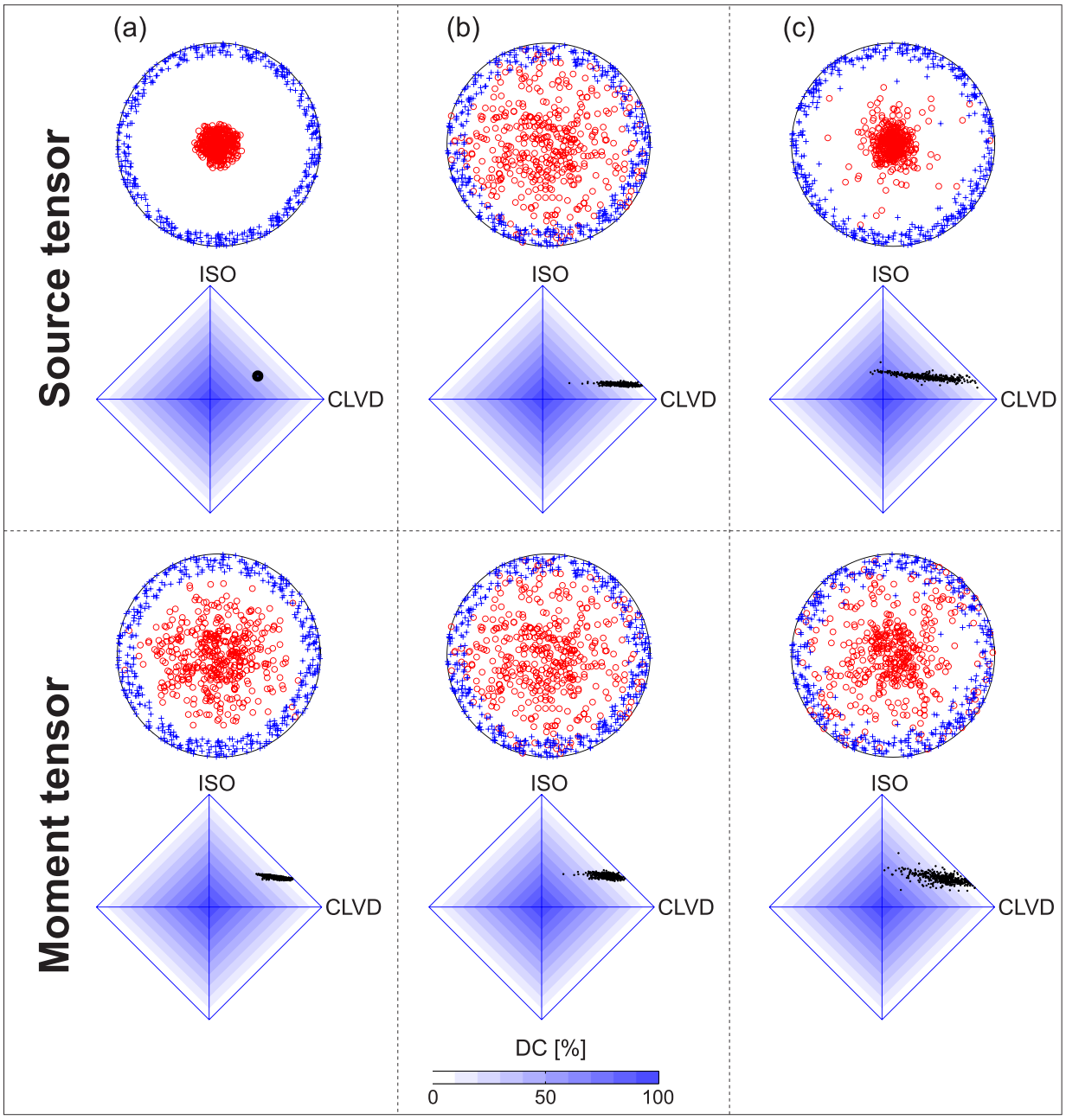

Figure 8. Synthetic tests of the moment and source tensor inversions of tensile AEs. The slope angle is ranging from 25° to 26°. The *P*-axes (red circles in focal spheres) and *T*-axes (blue plus signs in focal spheres) and the non-DC components (black dots in diamond plots) are calculated for the source tensors (upper plots) and moment tensors (lower plots) of AEs in (a) anisotropic attenuating model, (b) isotropic attenuating model and (c) anisotropic elastic model.

and vertical attenuations ranging from 0 to 9.4 $\times$ 10^{-3} s km^{-1} in steps of 2 $\times$ 10^{-4} s km^{-1}.

The results of the inversion are shown in Fig. 9. The rms function is smooth ranging between 0.069 and 0.348. The minimum rms is found for vertical attenuation of 3.2 $\times$ 10^{-3} and for horizontal attenuation of 5.8 $\times$ 10^{-3}. A good correspondence of the results with the true values indicates that the inversion is sufficiently robust and thus applicable to real observations. Similar results have also been obtained when calculating the misfit between the inverted and true amplitudes using the L1-norm instead of the standard L2-norm, and when 5 or 10 per cent of events with the highest rms (i.e. outliers) have been removed when calculating the mean rms.

5 APPLICATION TO LABORATORY DATA

5.1 Sensor calibration

Since measuring correct amplitudes is a key factor in determining accurate moment tensors, sensors of AEs must be carefully calibrated and coupling effects between the sensors and a specimen should be suppressed. We apply two methods for calibrating the AE sensors. First, the 'ultrasonic calibration' (Kwiatek *et al.* 2014b), which employs ultrasonic transmission data for evaluating sensor amplifications and coupling effects. Second, the 'network calibration' (Davi & Vavryčuk 2012; Davi *et al.* 2013), based on a

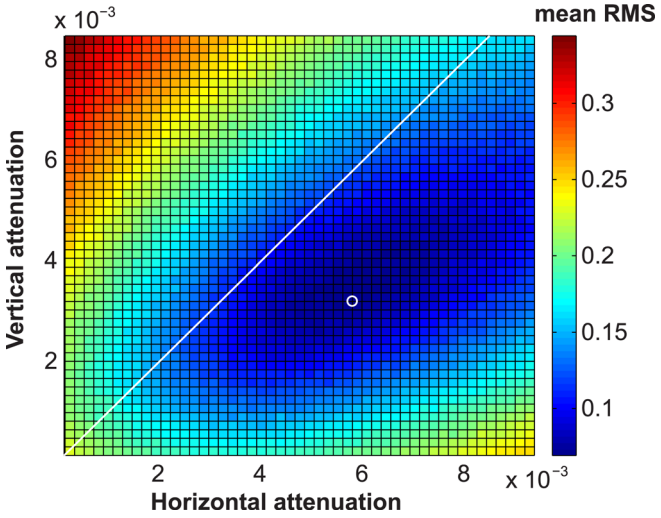

Figure 9. Synthetic test of the inversion for anisotropic attenuation. The mean rms value characterizes the mean fit of amplitudes in the moment tensor inversion for the synthetic AEs. The rms values are colour coded. The attenuation axes are in s km^{-1}. The optimum solution is marked by the white circle. The optimum rms is 0.069 for the horizontal attenuation of 5.8 $\times$ 10^{-3} s km^{-1} and the vertical attenuation of 3.2 $\times$ 10^{-3} s km^{-1}.

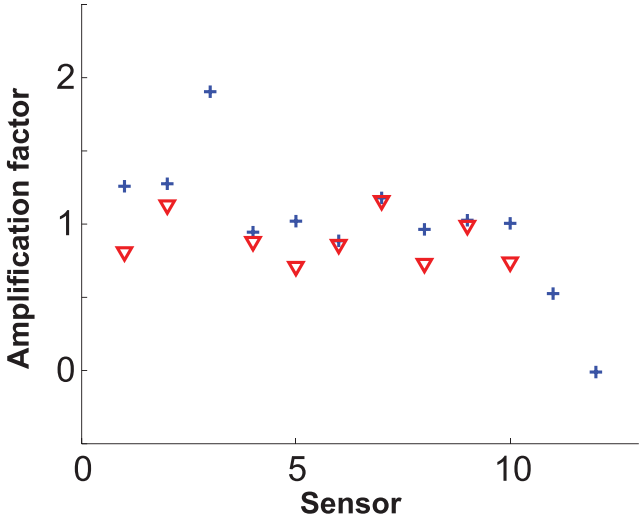

Figure 10. Calibration of sensors. Red triangles/blue plus signs show amplifications of sensors determined using the ultrasonic calibration (Kwiatek *et al.* 2014b) and the network calibration (Davi & Vavryčuk 2012), respectively. For sensors 3, 11 and 12, the amplifications of the ultrasonic calibration are missing, because the calibration was unstable.

joint inversion of many AE events for moment tensors and sensor amplifications.

Both methods yielded amplification factors ranging between 0.75 and 1.3 and detected no problems with coupling for 9 of 12 sensors (see Fig. 10). The other three sensors (sensors 3, 11 and 12) were calibrated just by the network calibration, because the ultrasonic calibration produced unstable results. The network calibration revealed that sensors 3 and 11 had slightly anomalous amplifications (1.4 and 0.5) and sensor 12 had a flipped polarity and amplification close to zero. Therefore, sensor 12 was excluded from the analysis and data recorded at the other sensors were corrected by the found amplifications.

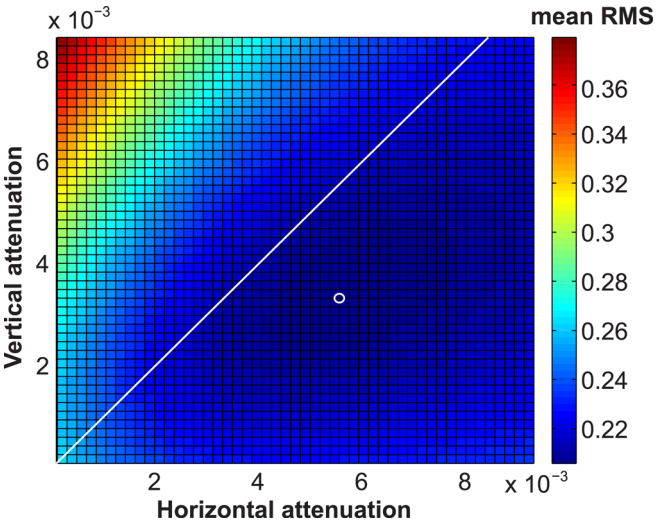

Figure 11. Inversion for anisotropic attenuation. The mean rms value characterizes the mean fit of amplitudes in the moment tensor inversion for observed AEs. The rms values are colour coded. The attenuation axes are in s km^{-1}. The optimum solution is marked by the white circle. The optimum rms is 0.21 for the horizontal attenuation of 5.6 $\times$ 10^{-3} s km^{-1} and the vertical attenuation of 3.4 $\times$ 10^{-3} s km^{-1}.

5.2 Inversion for anisotropic attenuation

The inversion for attenuation of the rock sample was run for a set of 429 of 1277 AEs, which occurred in the centre of the sample and displayed good coverage of sensors on the focal sphere (Fig. 4b). Amplitudes of AEs were picked using an automatic picking algorithm based on the Akaike information criterion (Leonard & Kennet 1999), and inverted for moment tensors by eq. (2). The inversion of the AEs was repeated for a set of anisotropic, attenuating models with fixed time-dependent velocity anisotropy and variable attenuation. The anisotropic velocity was taken from ultrasonic measurements (Fig. 3a) and the anisotropic attenuation varied in the same grid as in the synthetic test (Section 4.5). For each combination of the vertical and horizontal attenuations, we calculated the mean rms for the analysed dataset of AEs and searched for its minimum corresponding to the optimum anisotropic attenuation. We obtained a smooth 2-D function of rms with its minimum of 0.21 for the horizontal attenuation of 5.6 $\times$ 10^{-3} s km^{-1} and for the vertical attenuation of 3.4 $\times$ 10^{-3} s km^{-1} (Fig. 11). The sensitivity of the solution to the norm applied to calculating the misfit between observed and synthetic amplitudes (the L1- or L2-norm) and to the number of outliers was tested similarly as in the synthetic test (see Section 4.5). We found that the results are not changing and the solution remains stable.

Since attenuation in the rock sample is changing with increasing axial load, the inversion yields just a rough estimate of attenuation averaged over the loading cycle. Nevertheless, we clearly observe a higher value of attenuation in the horizontal direction compared to the vertical direction. This directional dependence is in good correspondence with ultrasonic measurements (Fig. 3d). During loading of the rock specimen, the horizontal cracks are closing and the pore space is compacted in the vertical direction. Consequently, elastic waves travelling in the vertical direction are less attenuated and the *P*-wave amplitudes as well as the P-wave velocities increase. By contrast, vertical cracks are opening causing a reduction of the *P*-wave amplitude and velocity and an increase in horizontal attenuation (i.e. direction parallel to the crack normal, see Hudson 1981). Also strain measurements show that dilatant cracking

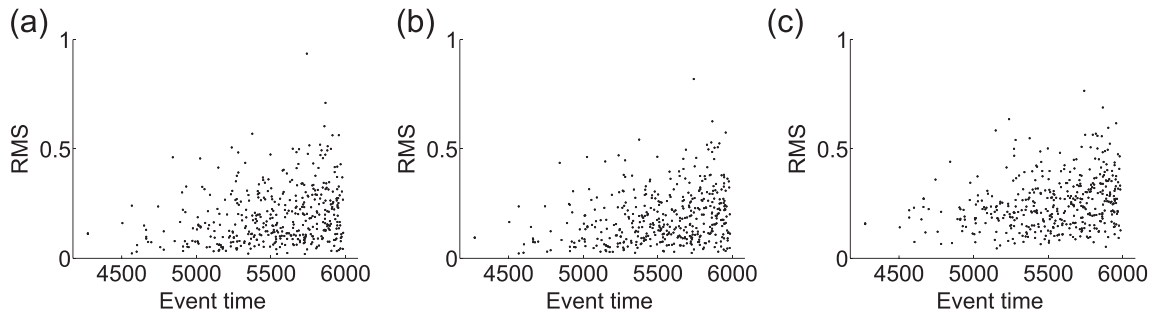

Figure 12. Root-mean-square (rms) values of the moment tensor inversion of observed AEs. The inversion is performed in: (a) the anisotropic attenuating medium, (b) the isotropic attenuating medium and (c) the elastic anisotropic medium.

becomes increasingly important in the horizontal direction (Stanchits *et al*. 2006).

5.3 Sensitivity of moment and source tensors to anisotropy and attenuation

Similarly as in the synthetic tests of the sensitivity of the moment and source tensors to anisotropy and attenuation (Section 4), we run the inversion of observed AEs using three medium models: anisotropic attenuating model, isotropic attenuating model and anisotropic elastic model. The parameters of velocity anisotropy of the sample are taken from ultrasonic measurements (see Fig. 3a). The attenuation parameters were time-dependent according to the measurements (see Fig. 3d) and scaled by values determined in the previous section: 5.6×10^{-3} and 3.4×10^{-3} s km^{-1} in the horizontal and vertical directions, respectively.

The results are as follows. First, rms values tend to increase with increasing axial load up to 0.5 independently of the medium model (Fig. 12). This increase probably reflects the continuous fracturing with increasing load, which is not fully described by the adopted homogeneous medium models. Second, neglecting the velocity anisotropy has a significant impact on the retrieved focal mechanisms. The P_S- and T_S-axes (Fig. 13b, upper plot) are highly scattered and geometry of faulting cannot be well resolved. By contrast, if anisotropy is considered and the source tensors correctly calculated (Figs 13a and c, upper plots), the P_S-axes are close to the vertical direction and the T_S-axes are nearly horizontal. This behaviour is physically reasonable and in correspondence with the applied stress regime. Third, the non-DC components of the moment and source tensors are rather stable in all three inversions (Fig. 13). The ISO and CLVD components are predominantly positive indicating that mainly tensile (opening) cracks were activated. The scatter in the CLVD component is higher than that in the ISO component as observed for the synthetic tests. This indicates that the errors in the velocity model mainly affect the CLVD component by producing their high scatter. Furthermore, the non-DC components of the source tensors are better clustered than the non-DC components of the moment tensors. In particular, the scatter in the ISO component of the source tensors is low.

To further assess the stability of the moment tensors we contaminated the observed amplitudes with uniformly distributed noise with a noise level reaching ±30 per cent of the observed amplitude at the respective sensor. For each event, 100 realizations were performed. The synthetic tests reveal a mean standard deviation of 8.7, 1.6 and 10.1 per cent for the DC, ISO, and CLVD components, respectively. The mean deviations of the P_M- and T_M-axes are 7.5° and 18°, respectively. Hence, the moment tensors are stable and the errors generated by noise are much lower than the errors generated by mismodelling of the rock properties such as by neglecting anisotropy or attenuation of the velocity model.

6 DISCUSSION AND CONCLUSIONS

Laboratory experiments are advantageous for the analysis of sensitivity of source and moment tensors to anisotropy and attenuation since: (1) they are carried out under controlled conditions and the physical parameters of the rock sample can be accurately monitored; (2) the sensors can be optimally distributed over the focal sphere; (3) the rock samples can display various levels of anisotropy and attenuation and (4) the loading of the rocks samples produces thousands of AEs needed for a thorough analysis with a statistical robustness. However, the determination of the moment and source tensors of AEs is also challenging in several aspects. The sensors need to be carefully calibrated and the AE sensor coupling problems should be eliminated. The number of sensors should be high and the recordings should have a sufficient dynamic range.

Synthetic tests and the laboratory measurements of AEs indicate that the moment and source tensors are quite sensitive to anisotropy and attenuation of the rock sample. Neglecting anisotropy and/or attenuation in the moment tensor inversion reduces the accuracy of the retrieved DC and non-DC components of the moment and source tensors. The errors in the non-DC components are mainly projected into the CLVD component which displays about three times higher scatter than the ISO component. Similar observations are reported by Stierle *et al*. (2014).

The errors produced by mismodelling of the medium also depend on the fracturing mode of AEs: tensile events are more sensitive to neglect of anisotropy and attenuation than shear events. This is explained by differences in the radiation pattern of shear and tensile sources. The radiation of a shear source has four lobes in isotropic media: two lobes of the positive polarity and two lobes of the negative polarity. The lobes are well-separated by nodal planes and constrain tightly the *P*- and *T*-axes. By contrast, the radiation pattern of a tensile source in isotropic media is axially symmetric and without nodes, predominantly with a single polarity. Consequently, the *P*- and *T*-axes are not well constrained being sensitive to deviations in amplitudes due to errors in the velocity model.

The presence of velocity anisotropy in a rock poses another complication. Geometry of faulting cannot simply be interpreted using the *P*- and *T*-axes of the moment tensors. These axes are affected by the velocity anisotropy and deviate from the true orientation of faulting. The stronger the anisotropy is, the higher the deviations are. This effect is eliminated by calculating and interpreting the *P*- and *T*-axes of the source tensors.

Finally, we proved that the moment tensor inversion applied to a large dataset of AEs could be utilized for determining the

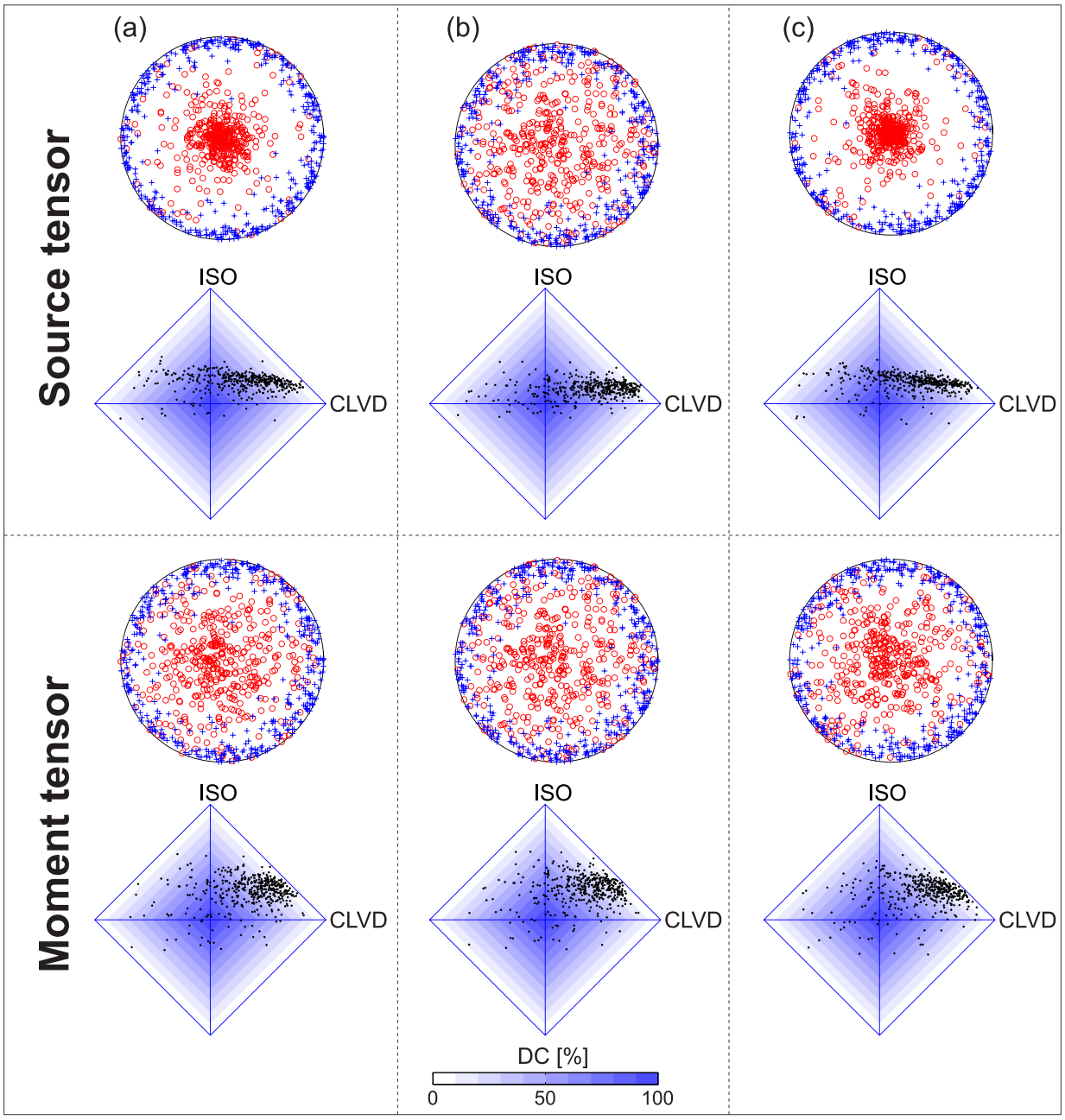

Figure 13. Moment and source tensor inversions of observed AEs. For meaning of the quantities, see the captions of Figs 6 and 8.

P-wave attenuation of the rock sample. The resolution of the method permits distinguishing between values of attenuation in the horizontal and vertical directions. The retrieved values are consistent with constraints on attenuation from independent ultrasonic measurements. The anisotropic attenuation with high values in the horizontal direction is explained by forming tensile cracks in the sample aligned along the vertical axial load applied to the specimen.

ACKNOWLEDGEMENTS

We thank the editor Jörg Renner and two anonymous reviewers for detailed and constructive reviews, and Sergei Stanchits for kindly providing data collected during his AE experiment on the granite specimen. This work was supported by the German Research Foundation (DFG) under the contract Bo1877/1-1 and by the Grant Agency of the Czech Republic, projects 210/12/1491 and 16-19751 J. We acknowledge funding from the Helmholtz-Foundation within the Young Investigator Group 'From microseismicity to large earthquakes'. The first author ES thanks the Christiane-Nüsslein-Volhard Foundation for co-funding.

REFERENCES

Aker, E., Kühn, D., Vavryčuk, V., Soldal, M. & Oye, V., 2014. Experimental investigation of acoustic emission and their moment tensors in rock during failure, *Int. J. Rock Mech. Min. Sci.,* **70,** 286–295.

Auld, B.A., 1973. *Acoustic Fields and Waves in Solids,* Wiley.

Ben-Zion, Y., 2003. Key formulas in earthquake seismology, in *International Handbook of Earthquake and Engineering Seismology,* pp. 1857–1875, eds Lee, W.H.K. *et al.*, Academic Press.

Bohnhoff, M., Dresen, G., Ellsworth, W.L. & Ito, H., 2009. Passive seismic monitoring of natural and induced earthquakes: case studies, future directions and socio-economic relevance, in *New Frontiers in Integrated Solid Earth Sci., Int. Yr. Planet Earth,* pp. 261–285, eds Cloetingh, S. & Negendank, J., Springer.

Carcione, J.M., 2007. *Wave Fields in Real Media: Wave Propagation in Anisotropic, Anelastic, Porous and Electromagnetic Media*, Elsevier.

Charalampidou, E.-M., Stanchits, S., Kwiatek, G. & Dresen, G., 2015. Brittle failure and fracture reactivation in sandstone by fluid injection, *Eur. J. Environ. Civ. Eng.,* **19**(5), 564–579.

Davi, R. & Vavryčuk, V., 2012. Seismic network calibration for retrieving accurate moment tensors, *Bull. seism. Soc. Am.,* **102**(6), 2491–2506.

Davi, R., Vavryčuk, V, Charalampidou, E.-M. & Kwiatek, G., 2013. Network sensor calibartion for retrieving accurate moment tensors of acoustic emissions, *Int. J. Rock Mech. Min. Sci.,* **62,** 59–67.

Finck, F., Kurz, J.H., Grosse, C. & Reinhardt, H.-W., 2003. Advances in moment tensor inversion for civil engineering, in *Proceedings of the Intern. Symp. Non-Destructive Testing in Civil Engineering (NDT-CE),* BB 85-CD, Berlin.

Graham, C.C., Stanchits, S., Main, I.G. & Dresen, G., 2010. Comparison of polarity and moment tensor inversion methods for source analysis of acoustic emission data, *Int. J. Rock Mech. Min. Sci.,* **47,** 161–169.

Hamiel, Y., Lyakhovsky, V., Stanchits, S., Dresen, G. & Ben-Zion, Y., 2009. Brittle deformation and damage-induced seismic wave anisotropy in rocks, *Geophys. J. Int.,* **178** (2), 901–909.

Helbig, K., 1994. *Foundations of Anisotropy for Exploration Seismics,* Pergamon.

Hudson, J.A., 1981. Wave speeds and attenuation of elastic waves in materials containing cracks, *Geophys. J. R. astr. Soc.,* **64,** 133–150.

Julian, B.R., Miller, A.D. & Foulger, G.R., 1998. Non-double-couple earthquakes. 1: Theory, *Rev. Geophys.,* **36,** 525–549.

Kwiatek, G., Plenkers, K. & Dresen, G., 2011. Source parameters of picoseismicity recorded at Mponeng deep gold mine, South Africa: implications for scaling relations, *Bull. seism. Soc. Am.,* **101**(6), 2592–2608.

Kwiatek, G., Goebel, T.H.W. & Dresen, G., 2014a. Seismic moment tensor and b value variations over successive seismic cycles in laboratory stick-slip experiments, *Geophys. Res. Lett.,* **41**(16), 5838–5846.

Kwiatek, G., Charalampidou, E.-M., Dresen, G. & Stanchits, S., 2014b. An improved method for seismic moment tensor inversion of acoustic emissions through assessment of sensor coupling and sensitivity to incidence angle, *Int. J. Rock Mech. Min. Sci.,* **65,** 153–161.

Lay, T. & Wallace, T.C., 1995. *Modern Global Seismology,* Academic Press.

Leonard, M. & Kennett, B.L.N., 1999. Multi-component autoregressive techniques for analysis of the seismograms, *Phys. Earth planet. Inter.,* **113**(1–4), 247.

Lockner, D., 1993. The role of acoustic-emission in the study of rock fracture, *Int. J. Rock Mech. Min. Sci.,* **30**(7), 883–889.

Ohtsu, M., 1991. Simplified moment tensor analysis and unified decomposition of acoustic emission source: application to in situ hydrofracturing test, *J. geophys. Res.,* **96,** 6211–6221.

Shigeishi, M. & Ohtsu, M., 2001. Acoustic emission moment tensor analysis: development for crack identification in concrete materials, *Constr. Build. Mater.,* **15,** 311–319.

Šílený, J. & Vavryčuk, V., 2000. Approximate retrieval of the point source in anisotropic media: numerical modelling by indirect parametrization of the source, *Geophys. J. Int.,* **143,** 700–708.

Šílený, J. & Vavryčuk, V., 2002. Can unbiased source be retrieved from anisotropic waveforms by using an isotropic model of the medium?, *Tectonophysics,* **356,** 125–138.

Stanchits, S., Lockner, D.A. & Ponomarev, A.V., 2003. Anisotropic changes in P-wave velocity and attenuation during deformation and fluid infiltration of granite, *Bull. seism. Soc. Am.,* **93**(4), 1803–1822.

Stanchits, S., Vinciguerra, S. & Dresen, G., 2006. Ultrasonic velocities, acoustic emission characteristics and crack damage of basalt and granite, *Pure appl. Geophys.,* **163**(5–6), 975–994.

Stanchits, S., Mayr, S., Shapiro, S. & Dresen, G., 2011. Fracturing of porous rock induced by fluid injection, *Tectonopysics,* **503,** 129–145.

Stierle, E., Vavryčuk, V., Šílený, J. & Bohnhoff, M., 2014. Resolution of non-double-couple components in the seismic moment tensor using regional networks: 1. A synthetic case study, *Geophys. J. Int.,* **196**(3), 1869–1877.

Thompson, B.D., Young, R.P. & Lockner, D.A., 2006. Fracture in Westerly granite under AE feedback and constant strain rate loading: nucleation, quasi-static propagation, and the transition to unstable fracture propagation, *Pure appl. Geophys.,* **163**(5–6), 995–1019.

Thompson, B.D., Young, R.P. & Lockner, D.A., 2009. Premonitory acoustic emissions and stick-slip in natural and smooth-faulted Westerly granite, *J. geophys. Res.,* **114,** doi:10.1029/2008JB005753.

Vavryčuk, V., 2004. Inversion for anisotropy from non-double-couple components of moment tensors, *J. geophys. Res.,* **109,** B07306, doi:10.1029/2003JB002926.

Vavryčuk, V., 2005. Focal mechanisms in anisotropic media, *Geophys. J. Int.,* **161,** 334–346.

Vavryčuk, V., 2007a. Ray velocity and ray attenuation in homogeneous anisotropic viscoelastic media, *Geophysics,* **72**(6), D119–D127.

Vavryčuk, V., 2007b. Asymptotic Green's function in homogeneous anisotropic viscoelastic media, *Proc. Roy. Soc. A,* **463,** 2689–2707.

Vavryčuk, V., 2008. Velocity, attenuation, and quality factor in anisotropic viscoelastic media: a perturbation approach, *Geophysics,* **73**(5), D63–D73.

Vavryčuk, V., 2011. Tensile earthquakes: Theory, modeling, and inversion, *J. geophys. Res.,* **116** (B12), B12320, doi:10.1029/2011JB008770.

Vavryčuk, V., 2015a. Moment tensor decompositionsrevisited, *J. Seismol.,* **19**(1), 231–252.

Vavryčuk, V., 2015b. Determination of parameters of viscoelastic anisotropy from ray velocity and ray attenuation: theory and numerical modelling, *Geophysics,* **80**(3), C59–C71.

Vavryčuk, V. & Yomogida, K., 1996. SH-wave Green tensor for homogeneous transversely isotropic media by higher-order approximations in asymptotic ray theory, *Wave Motion,* **23**(1), 83–93.

Zang, A., Wagner, F.C., Stanchits, S., Dresen, G., Andresen, R. & Heidecker, M.A., 1998. Source analysis of acoustic emissions in Aue granite cores under symmetric and asymmetric compressive loads, *Geophys. J. Int.,* **135,** 1113–1130.

Zang, A., Wagner, C., Stanchits, S., Janssen, C. & Dresen, G., 2000. Fracture process zone in granite, *J. geophys. Res.,* **105**(23), 651–661.